AFRL-AFOSR-JP-TR-2022-0037

Magnetometry of Novel 2-D Materials

Saha, Kasturi
INDIAN INSTITUTE OF TECHNOLOGY BOMBAY
POWAI
MUMBAI, , 400076
IN

05/31/2022
Final Technical Report

Air Force Research Laboratory
Air Force Office of Scientific Research
Asian Office of Aerospace Research and Development
Unit 45002, APO AP 96338-5002

REPORT DOCUMENTATION PAGE

PLEASE DO NOT RETURN YOUR FORM TO THE ABOVE ORGANIZATION.

1. REPORT DATE	2. REPORT TYPE	3. DATES COVERED	
20220531	Final	START DATE 20190905	END DATE 20220304

4. TITLE AND SUBTITLE
Magnetometry of Novel 2-D Materials

5a. CONTRACT NUMBER	5b. GRANT NUMBER	5c. PROGRAM ELEMENT NUMBER
	FA2386-19-1-4042	
5d. PROJECT NUMBER	**5e. TASK NUMBER**	**5f. WORK UNIT NUMBER**

6. AUTHOR(S)
Kasturi Saha

7. PERFORMING ORGANIZATION NAME(S) AND ADDRESS(ES)
INDIAN INSTITUTE OF TECHNOLOGY BOMBAY
POWAI
MUMBAI 400076
IN

8. PERFORMING ORGANIZATION REPORT NUMBER

9. SPONSORING/MONITORING AGENCY NAME(S) AND ADDRESS(ES)	10. SPONSOR/MONITOR'S ACRONYM(S)	11. SPONSOR/MONITOR'S REPORT NUMBER(S)
AOARD UNIT 45002 APO AP 96338-5002	AFRL/AFOSR IOA	AFRL-AFOSR-JP-TR-2022-0037

12. DISTRIBUTION/AVAILABILITY STATEMENT
A Distribution Unlimited: PB Public Release

13. SUPPLEMENTARY NOTES

14. ABSTRACT
Final Deliverable received 5/16/22

15. SUBJECT TERMS

16. SECURITY CLASSIFICATION OF:			17. LIMITATION OF ABSTRACT	18. NUMBER OF PAGES
a. REPORT	b. ABSTRACT	c. THIS PAGE		
U	U	U	SAR	9

19a. NAME OF RESPONSIBLE PERSON	19b. PHONE NUMBER *(Include area code)*
JERMONT CHEN	315-227-7003

Magnetometry of Novel 2D Materials

Kasturi Saha, Madhur Parashar, Anuj Bhatla, Dasika Shishir
Department of Electrical Engineering, Indian Institute of Technology Bombay, Powai, Mumbai-400076, India
(Dated: May 10, 2022)

I. INTRODUCTION

In the past couple of years several new two dimensional (2D) systems which show magnetic ordering have been discovered. These include crystalline atomic layers of CrTe, $CrTe_2$, $MnSe_2$, VSe_2, CrI_3, $FePS_3$, and $Cr_2Ge_2Te_6$. These systems provide an opportunity to study theoretical models such as the Ising transition, the Berezinskii–Kosterlitz–Thouless (BKT) transition, and the Mermin–Wagner model [1]. On the practical side, these magnetic states can be controlled through external interactions such as strain, light, electrical gating etc.. . Furthermore, novel quantum phases such as quantum Hall effect, quantum spin Hall effect, quantum spin liquids are expected to be present in these systems [2]. The success in understanding these *2D magnetic materials* and their technological utility critically relies on sensitive measurement techniques to probe them. It is especially desirable to do spatially resolved studies in contrast to bulk measurements.

Nitrogen vacancy(NV) centers in diamond can sense a wide range of physical quantities in both scanning and wide-field configurations. NV centers have been used to sense magnetic fields [3], temperature [4], electric fields [5], stress [6], and conductivity [7]. The scanning mode offers a high spatial resolution limited by the optical diffraction while the wide-field mode offers a fast simultaneous readout of a large measurement space at the cost of spatial resolution. Further, NV center based magnetometry works at a wide range of temperatures starting from 1 K [8] to 1000 K [9]. NV centers are non-magnetic point-like defects with no back action on the samples. This allows non-invasive sensing of a variety of materials ranging from thin superconducting films to magnetotactic bacterial cells.

NV center-based magnetometry has been extensively used to probe the magnetic state of 2D magnetic materials. L. Thiel et al. , (2019) [10], used scanning probe NV magnetometer to measure the magnetization of CrI_3 crystalline layers. An interesting dependence on the magnetic state and the number of layers (whether even or odd) was found. A similar study was done on $CrTe_2$ by F. Fabre et al. , (2021), [11]. McLaughlin et al. (2021) [12] used wide-field NV magnetometer to image exfoliated layers of Fe-chalcogenide. Fe-chalcogenide ($FeTe_xSe_{1-x}$) shows coexistence of superconducting and ferromagnetic phase under a critical temperature. Dynamic decoupling sequences extend the capabilities of NV center based magnetometry from DC sensing to AC sensing [13]. X.Y. Zhang et al. (2021) [14] made AC susceptibility measurements at a frequency of 200 kHz on $CrBr_3$ using XY-8 dynamical decoupling method. Another tool available using NV based quantum system is relaxometry [13]. In relaxometry, the T_1 coherence time of the spin is measured. The coherence time is effected by surrounding magnetic interactions, giving us valuable information about complex magnetic interactions. Lillie et al. , 2018 [15] examined broadband magnetic noise arising from various types of contamination of 2D films using T_1 relaxometry.

II. DEVELOPMENT OF QUANTUM DIAMOND MICROSCOPE

A. NV Magnetometry

In this section, we briefly describe the measurement protocol for measuring magnetic fields using NV centers in diamond. Several reviews can be found providing detailed description of quantum sensing and magnetometry [3, 16]. The negatively charged nitrogen vacancy center has $S = 1$ electron spin. The system has an excited state manifold that lies 1.945 eV (corresponding to a wavelength of 637 nm) above the ground state manifold. In the ground state manifold, $m_S = 0$ is the lower energy state and the near degenerate $m_S = \pm 1$ are the excited states. The energy difference between these spin sub-levels is $D = 2.87$ GHz, where D is called the *zero field splitting* parameter. In general, D is a function of temperature and the internal crystal strain. In the presence of external magnetic field $\mathbf{B}_{ext}$, the degeneracy between states $m_S = \pm 1$ is lifted. The spin Hamiltonian, $\mathcal{H}$, can be written as [3]

$$\frac{\mathcal{H}}{h} = DS_z^2 + E(S_x^2 - S_y^2) + \gamma_e \mathbf{B}_{ext} \cdot \mathbf{S}, \tag{1}$$

where $\gamma_e = g\mu_B/\hbar = 28\,\mathrm{MHz\,mT^{-1}}$ is the electron gyromagnetic ratio, and E is the crystal strain coupling, and S_x, S_y, S_z are the Pauli spin-1 matrices. Here z-axis is one of the four possible NV defect quantization axis in a diamond crystal as shown in Fig. 1. In the weak-field regime ($\gamma_e B_{perp} \ll D$),

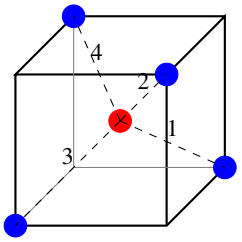

FIG. 1: Four possible orientations of NV-centers in a diamond crystals. The red circle depicts the vacancy and the blue circles depict the possible relative positions of nitrogen atoms with respect to the defect.

the electron spin resonance frequencies $\nu_\pm$ of Hamiltonian of

Eq. (1) are given by

$$\nu_{\pm} = D \pm \sqrt{E^2 + (\gamma_e B_z)^2}. \quad (2)$$

When $\gamma_e B_z \gg E$, the split in resonances can be further simplified as

$$\nu_{\pm} = D \pm \gamma_e B_z. \quad (3)$$

When excited by off-resonant green light (typically 532 nm), the NV center shows a spin dependent photo-luminescence (at 637 nm), where the state $m_S = 0$ is brighter than $m_S = \pm 1$ states [17]. By sweeping the microwave field and recording the photo-luminescence, one can obtain the magnetic field dependent resonant frequencies optically detected magnetic resonance (ODMR) as shown in Eq. (3). The typical field sensitivities obtained using the above mentioned protocol range from few tens of nT/$\sqrt{Hz}$ [18] to few tens μT/$\sqrt{Hz}$. The best reported sensitivity is 900 fT [19], for single point detection corresponding to 25 nT [19] per pixel in wide-field imaging. Imaging magnetic fields using NV center can be done in two modes. In a wide-field mode, the fluorescence from a diamond with high surface NV concentration is projected onto a CCD camera [20, 21] to reconstruct the magnetic field map. This mode offers a large field of view (few hundreds μm) in a time scale of a few minutes [20]. A lock-in camera can improve the signal-to-noise ratio by rejecting the phase incoherent parts of the PL. The total acquisition time from a lock-in camera can be reduced to a few seconds [22, 23]. The spatial resolution is however limited by the optical diffraction. In the scanning mode, a nano-fabricated diamond cantilever with a single NV center at the tip is used in an AFM-like experimental setup [24, 25]. This mode offers a high spatial resolution of few nano meters [25], and is ideal for probing sub-diffraction magnetic features. However, the scanning mode mechanism significantly increases the acquisition time and system complexity.

B. Experimental Setup

We have built a wide field setup that enables the imaging of a two-dimensional vector magnetic field from the sample. The excitation starts with a Lighthouse photonics Sprout-H 532 nm continuous laser adjustable upto 5 W [**1.** in Fig. 2]. The laser is passed through two halfwave plates (Thorlabs WPH10M-532) [**2.** in Fig. 2], which help in adjusting the polarization of the light. The output from the halfwave plate passes through a polarizing beam splitter (Thorlabs PBS102) [**3.** in Fig. 2]. A polarizing beam splitter reflects the s-polarized light at 45° angle and transmits the p-polarized light. Combined with the half-wave plate, this allows for a fine control of the laser output power. The laser beam is then passed through a telescopic lens combination which reduces the beam diameter. The narrow beam is passed through an acousto-optic modulator (AOM, Isomet M1133-aQ80L-H) [**4.** in Fig. 2]. Crystalline quartz optical medium present in the AOM is driven by 3.6 W, and 80 MHz RF signal to produce a controlled diffraction pattern. The first-order diffraction spot

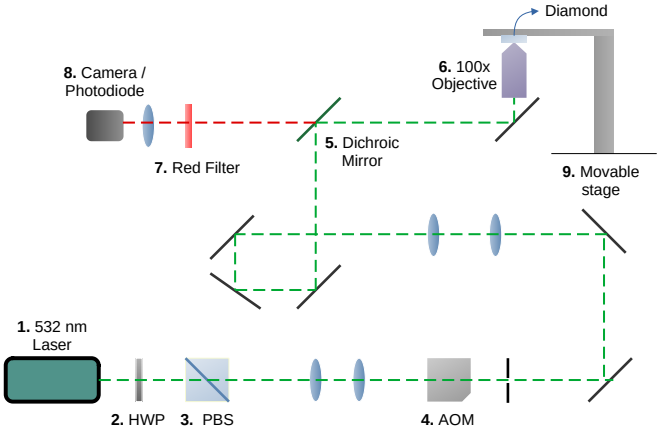

FIG. 2: Optical setup for magnetic field NV-center based magnetic field sensing experiments.

from the AOM is only present when the RF signal is enabled. By blocking the zeroth-order beam and with an iris (Thorlabs ID25), and allowing only the first-order beam we can obtain a switchable laser. The rise time of the laser was measured to be around 70 ns. All the switching, including the switching of RF signal for AOM, the microwave antenna is performed by a digital pulse generator (PulseBlasterESR-PRO). The first order spot is broadened again using a telescope lens combination, and is made to fall on a 100× objective (Olympus MPLFLN100X) [**6.** in Fig. 2]. On the other end of the objective, the diamond (procured from Element Six, with 1 ppm NV center layer of 1 µm thickness) is placed. The diamond is glued to the microwave antenna mentioned above. The red fluorescence from the diamond is collected through the same objective. In order to separate the red fluorescence from the excitation green laser, a dichroic mirror (Thorlabs DMLP567) [**5.** in Fig. 2] is placed, followed by optical long pass filters (Di03-R488/561-t1-25x36) [**7.** in Fig. 2].

The fluorescence data is collected through a photo-diode (Thorlabs DET102) [**8.** in Fig. 2], which is connected to a lock-in amplifier (SRS-850). The lock-in amplifier has an internal trans-impedance amplifier, with a gain of one million. In the case of wide-field imaging, a fast lock-in camera (Heliotis Helicam C3) is used. The lock-in camera can independently demodulate each pixel giving a microscopic image of the magnetic field.

Microwave signals in the range of 2.3 GHz to 3.2 GHz are provided by a microwave signal generator (SRS SG-380) [**1.** in Fig. 3]. The signal generator is equipped with Inphase-Quadrature (IQ) - modulation. IQ modulation is required for AC sensing protocols to control the phase of the microwave signals. The microwave signals are switched on of and off by a microwave switch (Miniciruits ZFSWA2-63DR+) [**2.** in Fig. 3]. The signal is provided to a microwave amplifier (Mini circuits ZHL-2W-63-S+)[**3.** in Fig. 3] with a 45 dB gain. Any reflections from the microwave due to impedance mismatches are prevented by a microwave circulator[**4.** in Fig. 3]. Finally the microwave power is delivered to a microstrip based omega antenna [**5.** in Fig. 3].

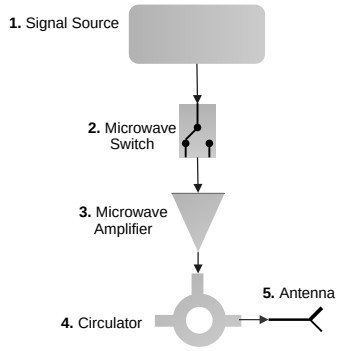

FIG. 3: Microwave path for magnetic field NV-center based magnetic field sensing experiments.

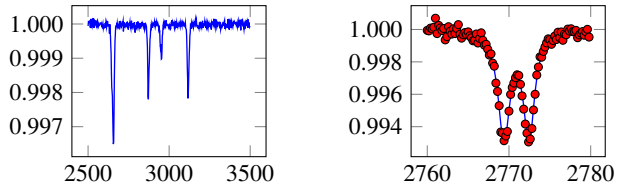

(a) ODMR spectrum with resonances from multiple NV orientations.

(b) Individual resonance with hyper-fines due to ^{15}N nucleus resolved.

FIG. 4: cw-ODMR spectrum of NV$^-$ center.

III. RESULTS

A. Continous Wave Experiments

In continuous wave experiments, microwave drive, laser excitation, and signal readout occur simultaneously. This technique called the continuous-wave optically detected magnetic resonance (cw-ODMR) is a simple and widely used technique for magnetic field sensing. The simplicity of this technique implies that it can be readily extended to a CCD camera for wide-field magnetic field imaging. In cw-ODMR, laser excitation continuously polarizes the NV-center into $m_S = 0$ state. When the microwave drive is resonant with $m_S = 0 \rightarrow \pm 1$, the states are driven to $m_S = \pm 1$ states. These states being less fluorescent than $m_S = 0$, state, result in a spectrum as shown in Fig. 4a. The four peaks correspond to four different NV$^-$ axis as shown in Fig. 1. Whenever the microwave frequency is resonant with $m_S = 0 \rightarrow \pm 1$ transition, there is a drop in the fluorescence. This drop is typically of a few percent below the baseline fluorescence. On a finer inspection of each resonant frequency, we find that each resonant frequency is split by the hyper-fine interaction between the NV$^-$ electrons and the spin-1/2 ^{15}N nucleus as shown in Fig. 4b. The splitting is usually around 3 MHz. Magnetic field sensitivity in cw-ODMR experiments is given by [26]

$$\eta_{cw} = \frac{4}{3\sqrt{3}} \frac{h}{g_e \mu_B} \frac{\Gamma}{C_{cw}\sqrt{R}}, \tag{4}$$

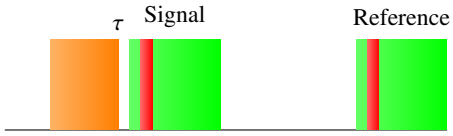

FIG. 5: Experimental protocol to obtain Rabi cycle. Orange is a microwave pulse, green is the laser excitation pulse, and red is photo-diode readout pulse. Contrast is measured as defined in Eq. (6).

.

with photon detection rate R, line-width Γ, cw-ODMR contrast C_{cw}, and the rest being the standard physical constants. In the experiments that we performed, the mean photo amplifier voltage was 0.2 V. The amplifier was set to a gain of 1×10^5 V A^{-1}. The responsivity of the photo-diode was 0.45 A W^{-1} at the NV-center resonance frequency of 637 nm. This implies that the rate of incident photons R was approximately 8.95×10^{13} s^{-1}. Using a spectral fit function $S(f, [c_1, f_1, \Gamma_1, c_2, f_2, \Gamma_2])$ that is a sum of two Lorentzian functions

$$S(f) = 1 - \frac{c_1}{1 + \left(\frac{f-f_1}{\Gamma_1/2}\right)^2} - \frac{c_2}{1 + \left(\frac{f-f_2}{\Gamma_2/2}\right)^2}, \tag{5}$$

where $c_{1,2}$, $\Gamma_{1,2}$, $f_{1,2}$ are the contrast, line-width, and resonant frequencies of the individual peaks, we extract the relevant parameters. For the spectrum shown Fig. 4b, we obtain the line-width Γ to be 1.7 MHz, and the contrast to be 0.006. From Eq. (5), the sensitivity turns out to be 0.7 nT/ $\sqrt{Hz}$.

B. Pulsed Experiments

In pulsed experiments, the electron spin evolves in the absence of excitation sources like light and microwave fields, with only the fields to be sensed being present. This reduces the effects of inhomogeneities that are present in the excitation sources and leads to enhanced sensitivity. Pulsed experiments are also essential for sensing AC fields.

1. *Rabi Oscillations*

Two levels of a quantum system $|0\rangle$, $|1\rangle$, show a cyclic behaviour in the presence of an oscillatory driving field $B_1 \sin \omega_\circ t$, known as the Rabi oscillations. To obtain a Rabi cycle, we first initialize the NV$^-$ state to $m_S = 0$ using a long laser pulse (around 5 µs). Then we sweep the resonant microwave excitation time τ as shown in Fig. 5. At resonance frequency, the Rabi oscillation frequency should be equal to $\Omega_R = \gamma_e B_1$. To obtain a contrast we measurement again with the microwave excitation off (*Reference*). The contrast is defined as

$$C_{rabi} = 1 + \frac{\text{Signal} - \text{Reference}}{\text{Signal} + \text{Reference}}, \tag{6}$$

with symbols Reference and Signal elaborated in Fig. 5. Rabi

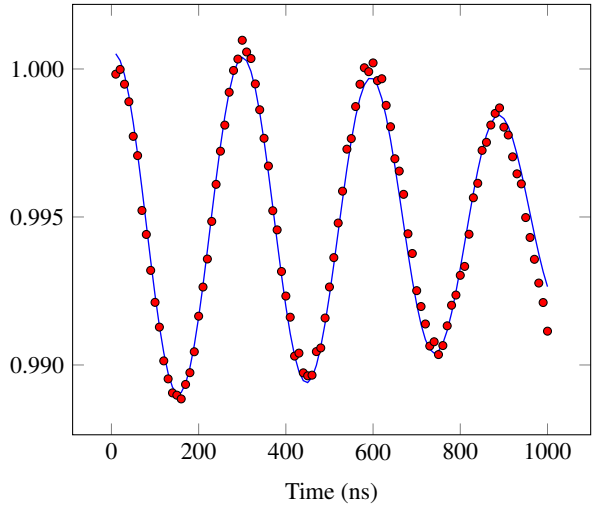

FIG. 6: Rabi cycle.

cycle that we obtained is shown in Fig. 6. The data obtained is fit to the following function

$$R(\tau;[C,T_d,T_R,\theta]) = 1 - C\exp\left(-\frac{t}{T_d}\right)\cos\left(\frac{2\pi}{T_R}(\tau-\theta)\right), \quad (7)$$

where C is the contrast, T_d is the decay due to inhomogeneous broadening, T_R is the Rabi cycle period, and θ is an auxiliary variable to account for small phase errors. The so called π and the $\pi/2$-pulse duration are defined as

$$t_\pi = \frac{T_R}{2}, \quad t_{\pi/2} = \frac{T_R}{4} \quad (8)$$

For the Rabi cycle shown in Fig. 6, the π-pulse duration is 130 ns, and the $\pi/2$-pulse duration is 65 ns. These durations signify the durations for which we need to apply microwave excitation to flip the spin from $|0\rangle$ to $|1\rangle$, $|0\rangle$ to a vector along transverse axis in the Bloch sphere respectively.

2. *Ramsey Fringes*

Ramsey method is used to sense static fields. In Ramsey experiment, the interaction of the qubit with sense field is segregated from microwave drive and laser excitation. In general, Ramsey method gives the best static field sensitivity. In the Ramsey method, the qubit is initialized to $|0\rangle$ using a long laser pulse.

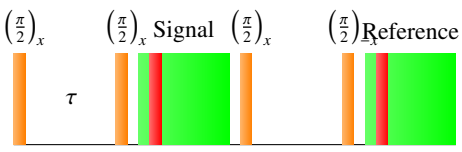

FIG. 7: Ramsey experiment protocol.

Then using microwave $\pi/2$-pulse, the qubit is rotated to transverse plane, with the spin state

$$\psi = \frac{1}{\sqrt{2}}(|0\rangle + |1\rangle) \quad (9)$$

After interacting with a static field which generates a de-tuning of $\Delta\omega$ for a duration τ, the spin evolves to

$$\psi = \frac{1}{\sqrt{2}}\left(|0\rangle + e^{-i\Delta\omega\tau}|1\rangle\right) \quad (10)$$

A final $\pi/2$ pulse converts the acquired phase to a population difference

$$\psi = \frac{1}{2}\left(1 + e^{-i\Delta\omega\tau}\right)|0\rangle + \frac{1}{2}\left(1 - e^{-i\Delta\omega\tau}\right)|1\rangle, \quad (11)$$

with a transition probability

$$p = 1 - |\langle 0|\psi\rangle|^2 = \frac{1}{2}\left[1 - \cos\left(\Delta\omega\tau\right)\right]. \quad (12)$$

The experimental protocol is illustrated in Fig. 7. Contrast is defined similar to Eq. (6). The Ramsey fringes we obtained at a de-tuning of 10 MHz are shown in Fig. 8. The data is fit to the function

$$R(\tau;[C,T_2^*,\Delta\omega,\theta]) = 1 - C\exp\left(-\frac{\tau}{T_2^*}\right)\cos\left(\Delta\omega\tau+\theta\right), \quad (13)$$

where C is the contrast, T_2^* is the transverse relaxation time, and θ is an auxiliary variable used to correct for phase errors. T_2^* signifies the time duration for which a qubit retains its coherence in the transverse plane. For the fringes shown in Fig. 8, T_2^* =380 ns. The shot-noise limited sensitivity of Ramsey method is [26]

$$\eta_{Ramsey} = \frac{\hbar}{g_e\mu_B}\frac{1}{C\sqrt{N_pT_2^*}}, \quad (14)$$

where C is the contrast, and N_p is the total photons collected. The total photons collected as the product of photon emission rate R and the collection time. In our experiment, the photon collection time is 500 ns. From Eq. (14), the shot noise sensitivity turns out to be 450 pT.

3. *Spin Echo and ESEEM*

The spin echo experiment is used to probe the environment of the spin. Spin environment is characterized by a decay time period T_2 called the spin-spin relaxation time. The pulse sequence used in the experiment is depicted in Fig. 9. The sequence consists of a $\pi/2-\tau-\pi-\tau-\pi/2$ sequence. The spin is initialized to $m_s = 0$ using a green laser pulse. This is followed by a $\pi/2$ pulse, which rotates the spin to a superposition of $m_s = 0$, and $m_s = 1$. The coherence in the superposition is lost due to the presence of spin-spin interactions. For common noise cancellation, the pulse sequence is applied twice. In the second sequence, the last $\pi/2$ pulse of the spin-echo is phase-shifted by 180° relative to the last $\pi/2$ pulse of the first. The contrast is calculated as difference over sum of these signals.

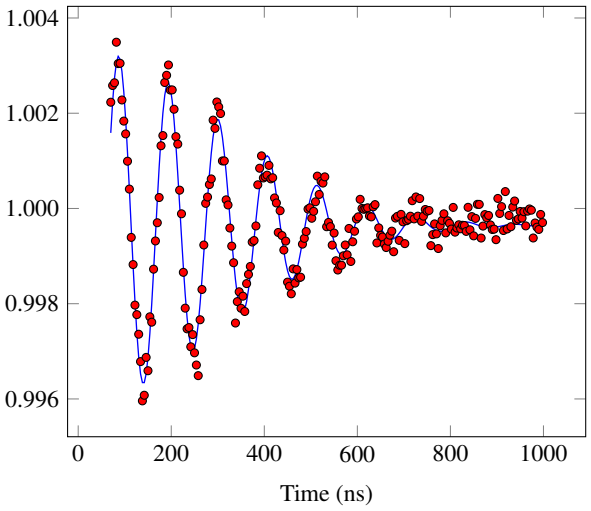

FIG. 8: Ramsey fringes.

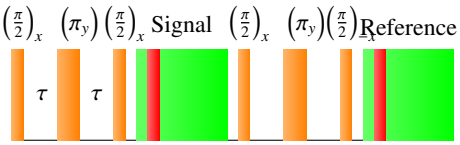

FIG. 9: Experimental protocol for Spin echo experiment.

The resultant signal, shown in Fig. 10 was fit to the following model function [27]

$$P_{echo}(t) = \exp\left(\frac{-t}{T_2}\right)\left[1 - \sin^2\phi \sin^2\frac{\omega_\circ t}{2}\sin^2\frac{\omega_1 t}{2}\right], \quad (15)$$

where $\omega_\circ$ is the envelop frequency, ω_1 is the modulation frequency, and T_2 is the decay time. These parameters turn out to be $\omega_\circ = 2\pi \times 238\,\mathrm{krad\,s^{-1}}$, $\omega_1 = 2\pi \times 3\,\mathrm{Mrad\,s^{-1}}$, and T_2 =7.89 µs. The modulation frequency is given approximately by [27]

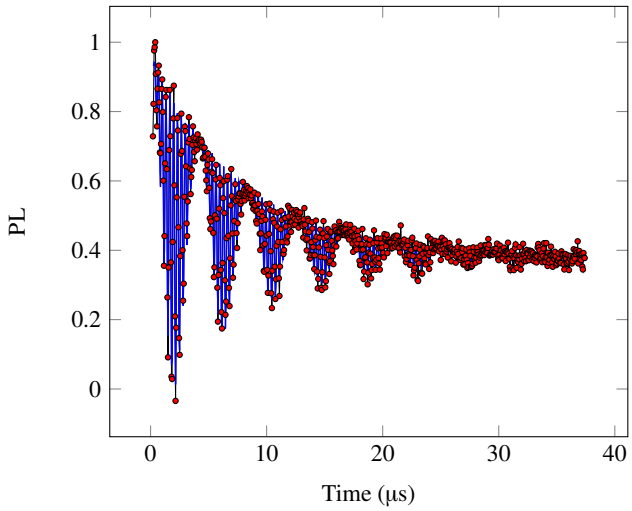

FIG. 10: ESEEM modulations in spin echo experiment.

$$\omega_1 \approx 2\pi \times [A_\parallel + \mu_n B_z], \quad (16)$$

where $A_\parallel$ is the parallel hyper-fine constant (3 MHz), μ_n is the nuclear Bohr magneton of 15N nucleus, and B_z is the field parallel to NV-axis. Because μ_n is small, the modulation frequency is generally close to the hyper-fine constant. The envelop frequency is given by [27]

$$\omega_0 \approx 2\pi \times [\gamma_{15N}/2\pi]\, B_\perp, \quad (17)$$

Substituting the values we obtained, the perpendicular field is around 3.9 mT and the parallel field (from CW-ODMR) is 2.5 mT. The 15N nucleus induces two modulation frequencies, the faster modulation frequency corresponds to the Larmor precession of the nucleus, and the envelop approximately proportional to the component of the external magnetic field perpendicular to the NV-center axis. The relaxation constant T_2 dictates the minimum AC magnetic-field frequency can be detected.

C. Widefield Magnetometry

In a wide-field magnetic microscope, we place a lock-in camera to collect the red photo-luminescence from the excited diamond. The camera is fitted with a 75 mm tube lens. The total optical magnification of the system is 33×. Each camera pixel size is 40 µm in size. Thus, light from 1.3 µm falls on 1 pixel of the lock-in camera. The microwave signal is frequency-shift keyed at a frequency of 6.25 kHz with a frequency deviation of 100 kHz. The resultant signal from a pixel of the camera at resonance is shown in Fig. 11. The signal shown in Fig. 11 is a derivative of sum of two Lorentzian functions. The interaction with a nearby ^{15}N nucleus leads to a hyperfine splitting of 3.05 MHz.

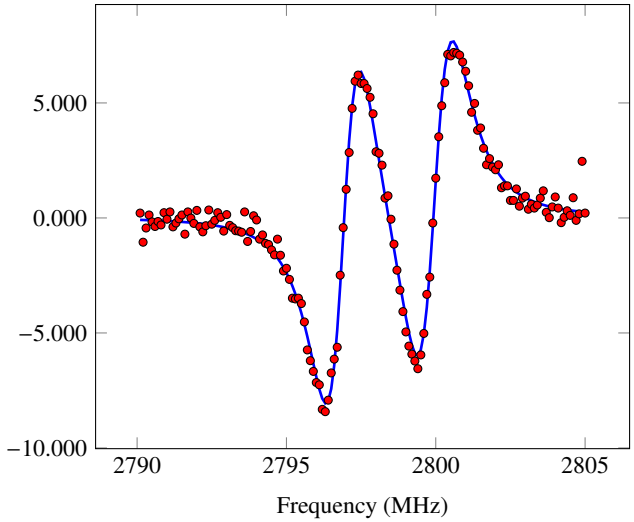

FIG. 11: Lock-in signal at NV resonance from an individual pixel of the lock-in camera.

To obtain a magnetic field map, we extract the resonance frequencies of each pixel and use Eq. (3) to get the magnetic field along a particular axis of that pixel. For a quasi-static magnetic field in a source-free region, Maxwell's equations require the field to be divergence and curl-free. With these two conditions imposed, one can reconstruct the entire vector field by knowing the field along any one axis. In the reciprocal domain, we have the relations

$$b_x(k_x, k_y) = \frac{-ik_x b_z(k_x, k_y)}{\sqrt{k_x^2 + k_y^2}} \tag{18}$$

$$b_y(k_x, k_y) = \frac{-ik_y b_z(k_x, k_y)}{\sqrt{k_x^2 + k_y^2}} \tag{19}$$

In a diamond crystal [111] direction has a unit vector $\left(\sqrt{2/3}, 0, \sqrt{1/3}\right)$, with respect to lab frame of reference. Thus, we can write

$$b_{111}(k_x, k_y) = \sqrt{\frac{2}{3}} b_x(k_x, k_y) + \sqrt{\frac{1}{3}} b_z(k_x, k_y). \tag{20}$$

By using Eq. (18) through Eq. (20), one can find all the magnetic field components from the field along a single NV axis. To verify and calibrate our magnetic microscope, we fabricated a 10 µm wide gold wire on top a silicon wafer using e-beam lithography and sputtering. We glued the silicon wafer to the diamond and passed a current of 10 µm through it. The vector magnetic field image from the sample is shown in Fig. 12. The magnetic field map matches the expectation of field profile from a current carrying wire.

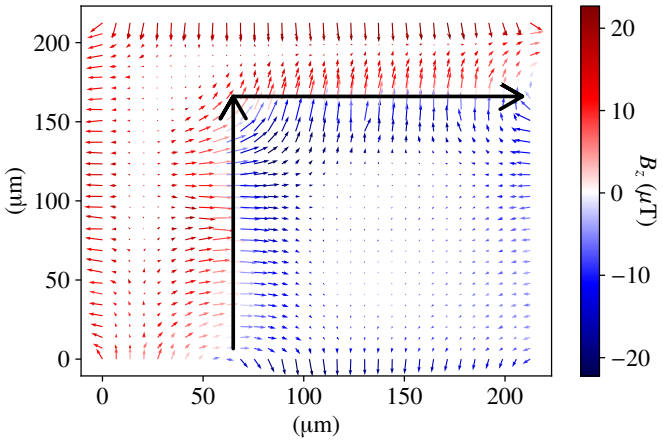

FIG. 12: Vector magnetic field map from a 10 µm current carrying wide gold wire. The black arrows represent the location of the gold wire.

We then demonstrated for the first time a wide-field magnetic field microscope capable of probing dynamically varying microscale magnetic field features at tunable imaging frame rates of 50-200 frames per second. In our demonstration we used planar microcoil sample with detailed microscale features, consisting of multiple current flow paths separated by ~ 7 µm, current flow track width 10 µm and multiple 90° turns in the current flow path. While maintaining microscale spatial resolution, individual pixels in the imaging view were shown to track applied magnetic fields in time with correct amplitude and phase for both periodic current waveforms and short 150 ms arbitrary current waveform. More details are available. In Fig. 13, we show magnetic field imaging of an arbitrary millisecond scale magnetic variation at 208 frames per second from the microcoil sample. The current signal here mimicks the current from a neuronal axon.

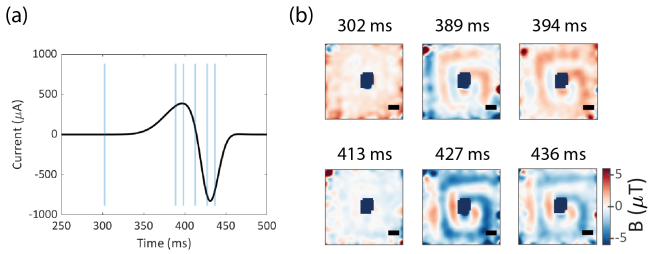

FIG. 13: Temporal imaging of an arbitrary millisecond scale magnetic field variation at 208 frames per second of the microcoil sample.

We also imaged the magnetic fields arising from 20 nm thick Nickel micro-magnets shown in Fig. 14a. In Fig. 14b, the variation in NV resonance frequency arising from the micro-magnet array is shown. Each micro-magnet has a dipolar kind of field as shown in Fig. 15a. The resultant was fit to a dipolar field

$$\mathbf{B}(\mathbf{m}, \mathbf{r}) = \frac{\mu_\circ}{4\pi} \frac{3(\mathbf{m} \cdot \hat{\mathbf{r}})\hat{\mathbf{r}} - \mathbf{m}}{r^3} \tag{21}$$

to extract the dipole moment and stand-off distance of the micro-magnets as shown in Fig. 15b. The dipole moment of each micro-magnet was found to be 1.3×10^{-13} J T^{-1}, with a stand-off distance of 13 µm.

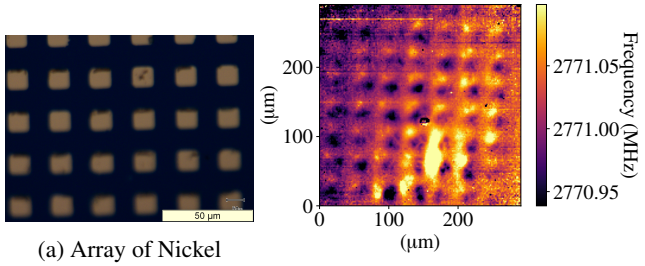

(a) Array of Nickel micromagnets.

(b) Resonance frequency map from an array of nickel micromagnets.

FIG. 14: Micro-magnet Array

IV. ACCOMPLISHMENTS

In a prior research work, published in Communication Physics (2020) [28], we have proposed a novel algorithm to

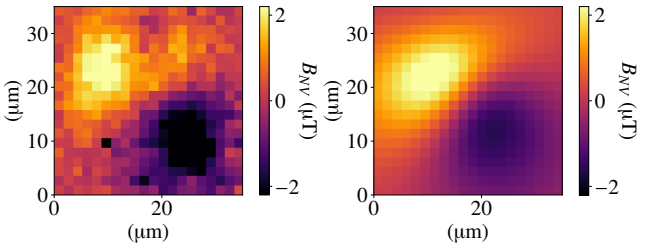

FIG. 15: Micro-magnet Array

reconstruct 3D magnetic field activity produced by action potentials (AP) of mammalian neurons located in a cortical volume. We have simulated the expected 2D microscale magnetic field patterns measured by diamond NV microscopy. In fundamental work by Roth *et. al* [29], it has been shown that 3D current source reconstruction is a non-unique inverse problem, unless additionally constrained with prior source information. Our analyses have shown that the axon hillock segment in the neuron provides a unique dominant signature to resolve neuronal activity in 3D with sufficient accuracy. Since AP magnetic fields are millisecond scale phenomena, our dynamic magnetic microscopy setup may enable us to probe novel AP associated magnetic fields at microscope resolution. In Ref. [30], we demonstrated for the first time a wide-field magnetic field microscope capable of probing dynamically varying microscale magnetic field features at tunable imaging frame rates of 50-200 frames per second.

V. FUTURE WORK

While the orginal proposal was intended to investigate 2D materials ar low temperature, the lack of funding for procuring the cryostat led us to focus on developing the room temperature quantum diamond microscope with the capability to investigate dynamic microscopic magnetic features. With the advent of room temperature 2D ferromagnetic materials, in the near future, we would like to use the capabilities of our wide-field magnetic microscope to investigate the properties of Ferromagnetic van der Waals (vdW) crystals. Although, most of the vdW compounds have a Curie temperature T_C well below 300 K, compounds of Chromium and Tellurium are known to show ferromagnetic order under ambient conditions as well [31]. In Fig. 16, magnetic field images of a $CrTe_2$ flake obtained using a scanning based NV magnetometer is shown by F Fabre et al. 2021 [11]. A quantitative estimate of the magnetization was obtained to be 27 kA m^{-1}. We would like to perform a similar characterization of these materials using the wide-field microscope described in previous sections. Despite the loss of spatial resolution while using a wide-field microscope, we can gain insight over a large field of view (of the order of hundreds of microns.). Not only would we like to do DC characterization, but extend the characterization to wide-field relaxometry and AC-sensing [32]. In this context we have recently interacted with Prof. Efren Navvaro for obtaining CrTe samples.

VI. PUBLICATIONS AND PATENTS

1. Parashar, M., Saha, K. & Bandyopadhyay, S. Axon hillock currents enable single-neuron-resolved 3D reconstruction using diamond nitrogen-vacancy magnetometry. *Commun Phys* **3**, 174 (2020).

2. Punyamoorty, V., Malusare, A., Sengupta, S., Pujari, S., & Saha, K. Size dependence in flux-flow Hall effect using time-dependent Ginzburg-Landau equations. *Phys. Rev. Research*, **3**, 033144 (2021).

3. Parashar, M., Bathla, A., Shishir, D., Gokhale, A., Bandyopadhyay, S., & Saha, K. Sub-second Temporal Magnetic Field Microscopy Using Quantum Defects in Diamond *arXiv [cond-mat.mes-hall]arXiv:2107.12232v2* (2021)(Accepted in Scientific Reports).

4. Shishir, D., Saha, K. Nitrogen vacancy centre-based diamond microscope for investigating quantum materials. *Bull Mater Sci* **44**, 276 (2021).

5. Patent filed:202121010532 filed at the Indian Patent Office.

VII. STUDENTS WHO HAVE BENEFITTED FROM THE FUNDING

1. Madhur Parashar

2. Anuj Bhatla

3. Dasika Shishir

REFERENCES

[1] K. S. Burch, D. Mandrus, and J.-G. Park, Magnetism in two-dimensional van der waals materials, Nature **563**, 47 (2018).

[2] M. Gibertini, M. Koperski, A. F. Morpurgo, and K. S. Novoselov, Magnetic 2d materials and heterostructures, Nature Nanotechnology **14**, 408 (2019).

[3] L. Rondin, J.-P. Tetienne, T. Hingant, J.-F. Roch, P. Maletinsky, and V. Jacques, Magnetometry with nitrogen-vacancy defects in diamond, Rep. Prog. Phys **77**, 056503 (2014).

[4] T. Plakhotnik, M. W. Doherty, J. H. Cole, R. Chapman, and N. B. Manson, All-optical thermometry and thermal properties

of the optically detected spin resonances of the nv– center in nanodiamond, Nano Lett. **14**, 4989 (2014).

[5] F. Dolde, M. W. Doherty, J. Michl, I. Jakobi, B. Naydenov, S. Pezzagna, J. Meijer, P. Neumann, F. Jelezko, N. B. Manson, and J. Wrachtrup, Nanoscale detection of a single fundamental charge in ambient conditions using the NV^- center in diamond, Phys. Rev. Lett. **112**, 097603 (2014).

[6] M. W. Doherty, V. V. Struzhkin, D. A. Simpson, L. P. McGuinness, Y. Meng, A. Stacey, T. J. Karle, R. J. Hemley, N. B. Manson, L. C. L. Hollenberg, and S. Prawer, Electronic properties and metrology applications of the diamond nv^- center under pressure, Phys. Rev. Lett. **112**, 047601 (2014).

[7] A. Ariyaratne, D. Bluvstein, B. A. Myers, and A. C. B. Jayich, Nanoscale electrical conductivity imaging using a nitrogen-vacancy center in diamond, Nat. Commun **9**, 2406 (2018).

[8] S. E. Lillie, D. A. Broadway, N. Dontschuk, S. C. Scholten, B. C. Johnson, S. Wolf, S. Rachel, L. C. L. Hollenberg, and J.-P. Tetienne, Laser modulation of superconductivity in a cryogenic wide-field nitrogen-vacancy microscope, Nano Lett. **20**, 1855 (2020).

[9] G.-Q. Liu, X. Feng, N. Wang, Q. Li, and R.-B. Liu, Coherent quantum control of nitrogen-vacancy center spins near 1000 kelvin, Nat. Commun **10**, 1344 (2019).

[10] L. Thiel, Z. Wang, M. A. Tschudin, D. Rohner, I. Gutiérrez-Lezama, N. Ubrig, M. Gibertini, E. Giannini, A. F. Morpurgo, and P. Maletinsky, Probing magnetism in 2d materials at the nanoscale with single-spin microscopy, Science **364**, 973 (2019), https://www.science.org/doi/pdf/10.1126/science.aav6926.

[11] F. Fabre, A. Finco, A. Purbawati, A. Hadj-Azzem, N. Rougemaille, J. Coraux, I. Philip, and V. Jacques, Characterization of room-temperature in-plane magnetization in thin flakes of $Crte_2$ with a single-spin magnetometer, Phys. Rev. Materials **5**, 034008 (2021).

[12] N. J. McLaughlin, H. Wang, M. Huang, E. Lee-Wong, L. Hu, H. Lu, G. Q. Yan, G. Gu, C. Wu, Y.-Z. You, and C. R. Du, Strong correlation between superconductivity and ferromagnetism in an fe-chalcogenide superconductor, Nano Letters **21**, 7277 (2021).

[13] C. L. Degen, F. Reinhard, and P. Cappellaro, Quantum sensing, Rev. Mod. Phys. **89**, 035002 (2017).

[14] X.-Y. Zhang, Y.-X. Wang, T. A. Tartaglia, T. Ding, M. J. Gray, K. S. Burch, F. Tafti, and B. B. Zhou, ac susceptometry of 2d van der waals magnets enabled by the coherent control of quantum sensors, PRX Quantum **2**, 030352 (2021).

[15] S. E. Lillie, D. A. Broadway, N. Dontschuk, A. Zavabeti, D. A. Simpson, T. Teraji, T. Daeneke, L. C. L. Hollenberg, and J.-P. Tetienne, Magnetic noise from ultrathin abrasively deposited materials on diamond, Phys. Rev. Materials **2**, 116002 (2018).

[16] R. Schirhagl, K. Chang, M. Loretz, and C. L. Degen, Nitrogen-vacancy centers in diamond: Nanoscale sensors for physics and biology, Annu. Rev. Phys. Chem **65**, 83 (2014), pMID: 24274702, https://doi.org/10.1146/annurev-physchem-040513-103659.

[17] H. Zhang, C. Belvin, W. Li, J. Wang, J. Wainwright, R. Berg, and J. Bridger, Little bits of diamond: Optically detected magnetic resonance of nitrogen-vacancy centers, Am. J. Phys **86**, 225 (2018), https://doi.org/10.1119/1.5023389.

[18] J. L. Webb, J. D. Clement, L. Troise, S. Ahmadi, G. J. Johansen, A. Huck, and U. L. Andersen, Nanotesla sensitivity magnetic field sensing using a compact diamond nitrogen-vacancy magnetometer, Appl. Phys. Lett. **114**, 231103 (2019), https://doi.org/10.1063/1.5095241.

[19] T. Wolf, P. Neumann, K. Nakamura, H. Sumiya, T. Ohshima, J. Isoya, and J. Wrachtrup, Subpicotesla diamond magnetometry, Phys. Rev. X **5**, 041001 (2015).

[20] S. Steinert, F. Dolde, P. Neumann, A. Aird, B. Naydenov, G. Balasubramanian, F. Jelezko, and J. Wrachtrup, High sensitivity magnetic imaging using an array of spins in diamond, Rev. Sci. Instrum. **81**, 043705 (2010), https://doi.org/10.1063/1.3385689.

[21] L. M. Pham, D. L. Sage, P. L. Stanwix, T. K. Yeung, D. Glenn, A. Trifonov, P. Cappellaro, P. R. Hemmer, M. D. Lukin, H. Park, A. Yacoby, and R. L. Walsworth, Magnetic field imaging with nitrogen-vacancy ensembles, New J. Phys. **13**, 045021 (2011).

[22] M. Parashar, D. Shishir, A. Gokhale, A. Bathla, S. Bandyopadhyay, and K. Saha, Per pixel lock in detection based dynamic widefield magnetometry using quantum defects in diamond, Bulletin of the American Physical Society (2021).

[23] A. M. Wojciechowski, M. Karadas, A. Huck, C. Osterkamp, S. Jankuhn, J. Meijer, F. Jelezko, and U. L. Andersen, Contributed review: Camera-limits for wide-field magnetic resonance imaging with a nitrogen-vacancy spin sensor, Rev. Sci. Instrum. **89**, 031501 (2018), https://doi.org/10.1063/1.5010282.

[24] T. X. Zhou, R. J. Stöhr, and A. Yacoby, Scanning diamond nv center probes compatible with conventional afm technology, Appl. Phys. Lett **111**, 163106 (2017), https://doi.org/10.1063/1.4995813.

[25] P. Appel, E. Neu, M. Ganzhorn, A. Barfuss, M. Batzer, M. Gratz, A. Tschöpe, and P. Maletinsky, Fabrication of all diamond scanning probes for nanoscale magnetometry, Rev. Sci. Instrum. **87**, 063703 (2016), https://doi.org/10.1063/1.4952953.

[26] J. F. Barry, J. M. Schloss, E. Bauch, M. J. Turner, C. A. Hart, L. M. Pham, and R. L. Walsworth, Sensitivity optimization for nv-diamond magnetometry, Rev. Mod. Phys. **92**, 015004 (2020).

[27] B. A. Myers, *Quantum decoherence of near-surface nitrogen-vacancy centers in diamond and implications for nanoscale imaging* (University of California, Santa Barbara, 2016).

[28] M. Parashar, K. Saha, and S. Bandyopadhyay, Axon hillock currents enable single-neuron-resolved 3d reconstruction using diamond nitrogen-vacancy magnetometry, Communications Physics **3**, 174 (2020).

[29] B. J. Roth, N. G. Sepulveda, and J. P. Wikswo, Using a magnetometer to image a two-dimensional current distribution, Journal of Applied Physics **65**, 361 (1989), https://doi.org/10.1063/1.342549.

[30] M. Parashar, D. Shishir, A. Bathla, A. Gokhale, S. Bandyopadhyay, and K. Saha, Lock-in detection based dynamic widefield magnetometry using quantum defects in diamond (2021), arXiv:2107.12232 [cond-mat.mes-hall].

[31] X. Zhang, Q. Lu, W. Liu, W. Niu, J. Sun, J. Cook, M. Vaninger, P. F. Miceli, D. J. Singh, S.-W. Lian, T.-R. Chang, X. He, J. Du, L. He, R. Zhang, G. Bian, and Y. Xu, Room-temperature intrinsic ferromagnetism in epitaxial crte2 ultrathin films, Nature Communications **12**, 2492 (2021).

[32] K. Mizuno, H. Ishiwata, Y. Masuyama, T. Iwasaki, and M. Hatano, Simultaneous wide-field imaging of phase and magnitude of ac magnetic signal using diamond quantum magnetometry, Sci Rep. **10**, 11611 (2020).

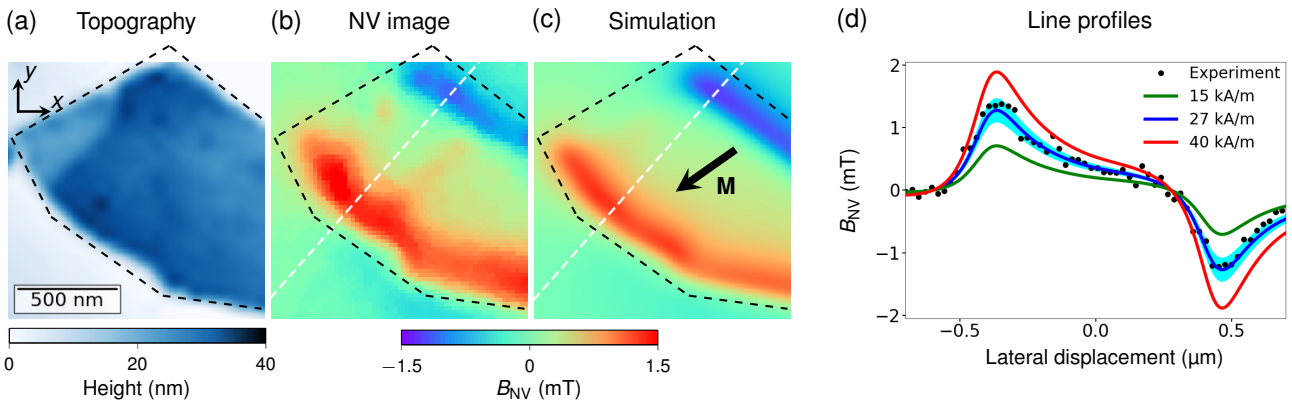

FIG. 16: (a) AFM topography of $CrTe_2$ flake. (b) Magnetic field image obtained from scanning probe. (c) Simulated field image. [Adapted from [11]]